Soil Deposition of Atmospheric Hydrogen Constrained using Planetary Scale Observations

Alexander K. Tardito Chaudhri[1] and David S. Stevenson[1]

[1]The University of Edinburgh, King's Buildings, Alexander Crum Brown Rd, Edinburgh EH9 3FF

Correspondence: Alexander K. Tardito Chaudhri (achaudH2@ed.ac.uk)

Abstract. Quantifying soil deposition fluxes remains the greatest source of uncertainty in the atmospheric H_2 budget. A new method is presented to constrain H_2 deposition schemes in global models using observations of the zonal mean H_2 distribution and seasonality. A 'best-fit' scheme that reproduces the observed zonal-mean seasonality of atmospheric H_2 at the planetary scale is found by perturbing a prototype deposition scheme based on soil temperature and moisture dynamics. Comparing the best-fit and prototype schemes provides insight for how the prototype scheme may be improved to better reproduce observed seasonality.

The H_2 signal driven by the prototype scheme is accurate compared to observations in the Northern Hemisphere extra-tropics but shows discrepancies in the Southern Hemisphere, with too high surface mixing ratios and too weak seasonality. A best-fit scheme indicates that the function capturing the soil microbial consumption of H_2 requires a shift of approximately +3 months in the seasonality in the tropics, where the prototype scheme is sensitive to seasonal soil moisture driven by the shifting of the ITCZ. New constraints on the H_2 surface flux at low-latitudes are key to accurately modelling the H_2 cycle in the Southern Hemisphere.

1 Introduction

In recent years there have been widespread announcements of new plans for hydrogen energy systems (Warwick et al., 2023). As such, future hydrogen emissions are expected to increase, in large part due to fugitive emissions from infrastructure (Ocko and Hamburg, 2022; Esquivel-Elizondo et al., 2023). Although the symmetrical H_2 molecule is not itself a greenhouse gas, its presence depletes atmospheric OH that would otherwise oxidise methane (Warwick et al., 2023). Hydrogen oxidation by OH additionally contributes the greenhouse gases ozone and water, with the latter having a significant warming effect in the otherwise dry stratosphere (Sand et al., 2023; Warwick et al., 2023). However, despite the increasing number of modelling studies that have provided new insights into the atmospheric chemistry of H_2, there remain large uncertainties in evaluations of the Global Warming Potential (GWP) of H_2 (Sand et al., 2023; Derwent, 2023). Different recent estimates for the GWP over a 100 year time horizon include: Sand et al. (2023), 11.6 ± 2.8; Derwent (2023), 7.1-9.3; and Warwick et al. (2023), 12 ± 6.

Quantifying the soil sink, and its counterpart H$_2$ emissions, have remained the main source of uncertainty in the atmospheric
H$_2$ budget (cf. Novelli, 1999; Sand et al., 2023) and hence the lifetime of H$_2$, which generates large uncertainty in the GWP
calculations that are relied on for understanding the climate impacts of H$_2$ applications.

Present-day (2010s) surface H$_2$ mixing ratios are c.550 ppb (Pétron et al., 2023), and showed an increasing trend of about
2.5 ppb yr^{-1} in the latter part of the 20th century (Patterson et al., 2020). However, the origin of the increase is unclear.
H$_2$ concentrations show a distinct latitudinal variation, with values about 50 ppb higher in the Southern Hemisphere (SH)
compared to Northern Hemisphere (NH) high-latitudes. They also show a characteristic seasonal cycle; outside the tropics H$_2$
generally peaks in the summer, with a monthly mean peak-to-peak magnitude of 30-60 ppb in the NH and 15-30 ppb in the
SH.

To produce the same observed atmospheric H$_2$ concentrations, a stronger soil sink implies greater emissions and a shorter
atmospheric lifetime (Hauglustaine et al., 2022; Ehhalt and Rohrer, 2013; Sand et al., 2023). In a comparison of six atmospheric
chemistry models with imposed boundary layer H$_2$ concentrations, Sand et al. (2023) evaluated an uncertainty contribution to
the GWP of 18% of the mean due to uncertainty in the soil sink.

While constraining the annual mean planetary soil sink constrains the lifetime of H$_2$ in the bulk atmosphere, the observational
data contains additional useful information about the latitudinal distribution and seasonal variation of H$_2$, that we exploit here.
We filter these observations to decompose the observed H$_2$ signal into a 2012-2018 mean background state and a seasonal
cycle (Sec. 2).

Several different deposition schemes to model the soil sink of H$_2$ exist (e.g. Sanderson et al., 2003; Paulot et al., 2021; Ehhalt
and Rohrer, 2013; Bertagni et al., 2021). These schemes are typically based on laboratory or field studies of a small number of
deposition flux samples (e.g. Yonemura et al., 2000; Meredith et al., 2014) and model deposition velocities with functions of
soil texture, water content, and temperature. There are also indications that soil carbon content is important in determining the
H$_2$ deposition velocity (Khdhiri et al., 2015; Karbin et al., 2024). Here we provide a method to evaluate deposition schemes
at the planetary scale. Observational data of surface H$_2$ measurements provides time-series of surface mixing ratios from
a globally distributed set of sites (Pétron et al., 2023). We extend previous analysis of the seasonality of individual station
measurements (Novelli, 1999) and on the combined roles of tropical biomass burning, deposition, and convective uplift in
contributing seasonal variation (Hauglustaine and Ehhalt, 2002; Yashiro et al., 2011), through an analysis that accounts for the
continuous variation of seasonality with latitude. This extends the work of Xiao et al. (2007), who decomposed H$_2$ sources and
sinks based on the seasonality in tropical and extra-tropical regions.

The annual-mean distribution and seasonality of H$_2$ concentration are controlled by surface emissions and deposition, pro-
duction and loss by atmospheric chemistry and by atmospheric transport. Due to the slow response of relatively well mixed
H$_2$ in the atmosphere, with lifetime ~2 years (see Ehhalt and Rohrer, 2009; Patterson et al., 2020; Warwick et al., 2023; Sand
et al., 2023), we assume that the general effect of these fluxes is well approximated when they are modelled in their zonal-mean
monthly-mean.

Beginning with an analysis of the observed H$_2$ distribution and seasonality (Sec. 2), we then introduce a prototype deposition
scheme based on formulations of the moisture and temperature dependence of soil biology and diffusion processes (Sec. 3).

This is included in a toolbox model (Sec. 4) with best-estimates of: emissions with a spatial and monthly signal determined by
60 Paulot et al. (2021) with strength and atmospheric chemistry estimated by Sand et al. (2023); and tropospheric transport ide-
alised as a latitude-height overturning from ERA5 monthly mean wind speeds (Hersbach et al., 2020) and diffusion parameters
tuned based on reproducing the observed SF_6 distribution. By comparing the simulated H_2 concentration against the observed
distribution and seasonality we determine new constraints on the soil deposition as a function of latitude that we apply to tune
the original prototype scheme (Sec. 5).

65 **2 Filtering and Decomposition of H_2 Observations**

Timeseries of H_2 mixing ratios (Pétron et al., 2023) have been measured at the NOAA Global Monitoring Laboratory from
flask samples received from a latitude spanning network of sites (NOAA Global Monitoring Laboratory, 2024). These flask
samples have typically been taken once or twice weekly since 2010 (Pétron et al., 2023) using a portable sampling unit with
a c.5m mast, and samplers are instructed to preferably sample upwind of buildings at times when wind speeds are $\geq 2\ \text{ms}^{-1}$
70 (NOAA Global Monitoring Laboratory, 2005).
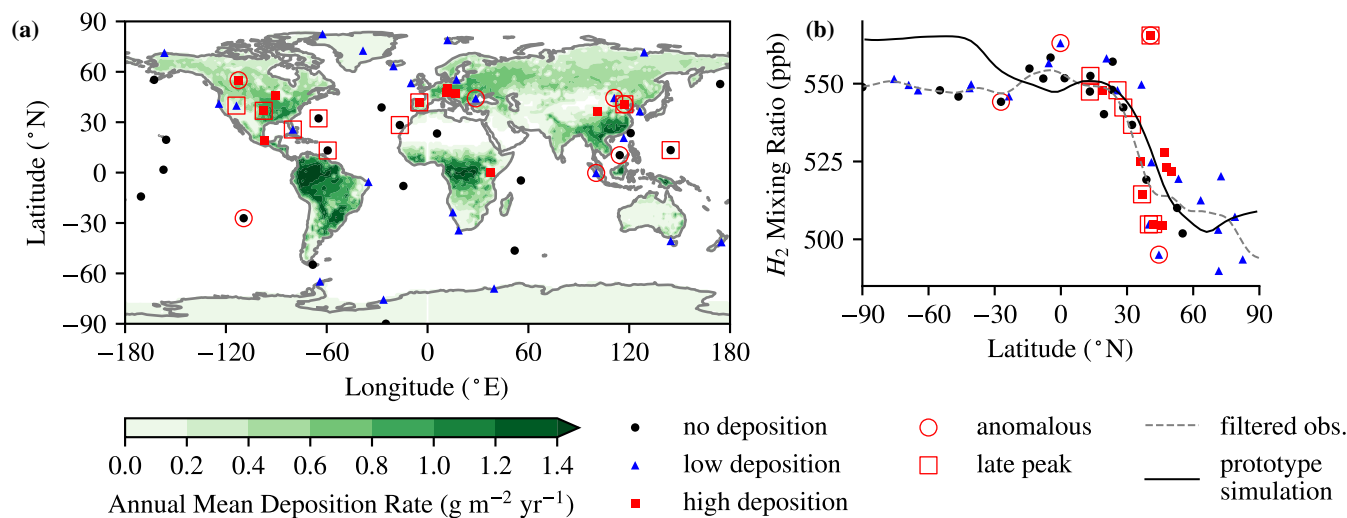
Figure 1. (a) Annual mean H_2 deposition flux (g m^{-2} yr^{-1}) in the prototype deposition scheme (shading), with surface H_2 measuring
stations (symbols) (NOAA Global Monitoring Laboratory, 2024) filtered by local deposition in the prototype deposition scheme (Table 1).
(b) observed 2012-2018 mean H_2 mixing ratio at surface measuring sites (symbols) (Pétron et al., 2023) and the near-surface zonal model
results from a simulation using the prototype deposition scheme (solid line). Anomalous sites are determined based on RMS error of the sum
of the first and second harmonics versus with the mid-filtered station time-series; $\sqrt{\sum_t \left(h_1 + h_2 - F_{mid}(\text{data})\right)^2} > 20$ ppb (circled, Fig.
3). A cluster of sites in the NH subtropics have a peak in the first harmonic after 150 days (squared, in Fig. 3 peak 1-2 months later than
other sites in the sub-tropics). Filtered observations (grey dashed line) is a fit to the observational data excluding anomalous stations (circled)
using a Gaussian filter with $\sigma = 5°$lat.
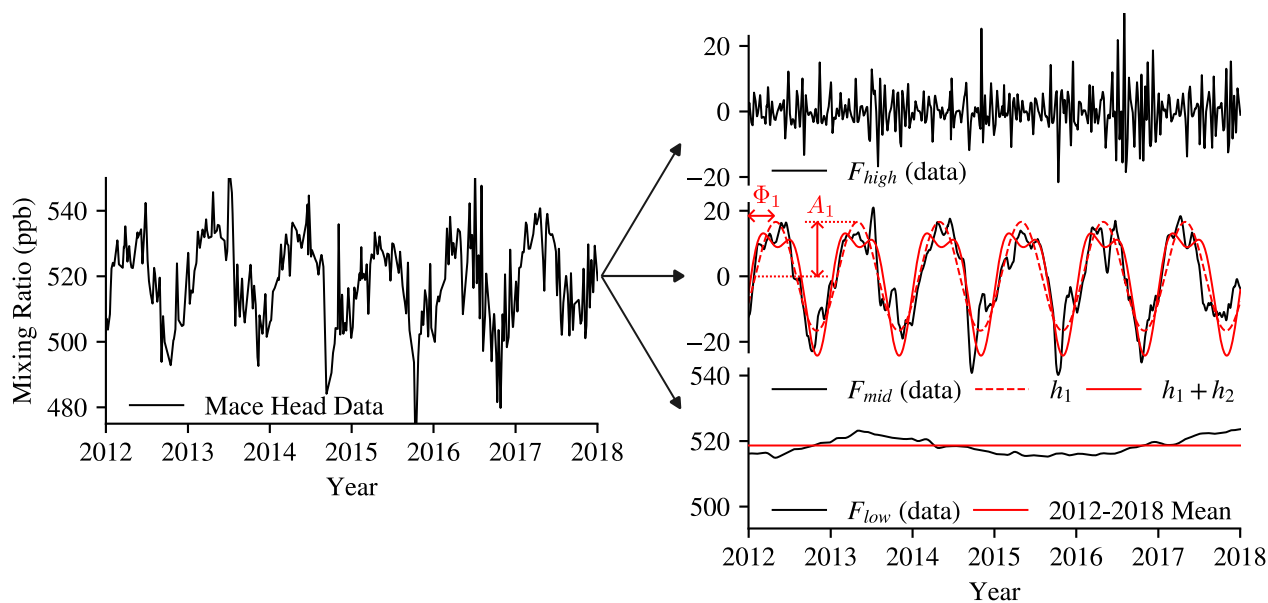
Figure 2. Example decomposition of the 2012-2018 H_2 observations from the Mace Head atmospheric research station (left) (Pétron et al., 2023) into: top-right, high-frequency noise on timescales < 30 days (F_{high}); mid-right, seasonality on timescales 30 days - 1 year (F_{mid}), with first (h_1) and second (h_2) harmonics fitted to this (red solid and dashed lines respectively); bottom-right, the residual inter-annual variation (F_{low}); and the 2012-2018 mean (red line). The amplitude, A_1, and phase, Φ_1, of the first harmonic are indicated.

We apply a spatial filtering to the measurement sites based on the predicted annual mean deposition rate in the biophysics based prototype deposition scheme that we introduce in Sec. 3 (Fig. 1a). By drawing a systematic comparison across sites we are able to extract general features of the planetary signal of background surface H_2 distribution and seasonality.

Additional to the spatial filtering of sites, temporal filtering is used to decompose how the observed H_2 signal varies over
75 different timescales. We analyse the seasonality at each site then compare these signals across latitudes rather than finding the seasonality of latitude-clustered sites (c.f. Paulot et al., 2024), restricting our analysis to a set of station measurements where consistent sampling exists in the period 2012-2018.

We implement a filter F_{mid} to isolate the seasonal cycle. F_{mid} returns the recorded data minus the high-frequency noise isolated with a high-pass filter, F_{high}, and the inter-annual variation isolated with a low-pass filter, F_{low}. This decomposition is
80 illustrated for data recorded at the Mace Head atmospheric research station in Fig. 2. High-frequency noise driven by synoptic weather occurs on timescales < 30 days and is isolated with F_{high} by subtracting a central moving average with a 30 day window from the data. Subtracting the high-frequency noise from the data reveals a background state where the remaining temporal variation is dominated by a seasonal cycle (Paulot et al., 2024). Therefore, to isolate the low-frequency inter-annual variability and trends it is suitable to define F_{low} as a central moving average with a 1 year window.

85 This background state reveals the trend of increasing atmospheric burden varying on timescales $\tau_{low} \geq 1$ year (Novelli, 1999; Patterson et al., 2020; Ehhalt and Rohrer, 2013). Furthermore, the meridional gradient of its mean state (Fig. 1b), combined

with quantification of the atmospheric production and loss of H_2, reveals the net surface fluxes in either hemisphere (Sanderson et al., 2003).

The first harmonic of the seasonality at each site (Fig. 3a,b) is identified by optimising the fit of the curve

$$h_1(A_1, \Phi_1) = A_1 \cos\big(\Omega(t - \Phi_1)\big) \tag{1}$$

to the F_{mid} filtered data, where A_1 and Φ_1 are, respectively, the amplitude and phase of the harmonic (illustrated for Mace Head in Fig. 2), and $\Omega = 2\pi \ \mathrm{yr}^{-1}$. Additionally, a second harmonic of the seasonality is identified by optimising the fit of

$$h_2(A_2, \Phi_2) = A_2 \cos\big(2\Omega(t - \Phi_2)\big) \tag{2}$$

to the F_{mid} filtered data minus h_1 (Fig. 3c,d).

The accuracy of describing the seasonality with A_1, Φ_1, A_2, Φ_2 at each site is assessed by considering the root-mean-square (RMS) error of $h_1 + h_2$ minus the F_{mid} filtered data. Anomalous results are categorised where this RMS error is greater than 20 ppb.

Between 2012 and 2018 both the annual mean surface H_2 mixing ratio (Fig. 1b) as well as the amplitude (Fig. 3a) and phase (Fig. 3b) of the seasonal variability – the time of the peak of the first harmonic of the seasonal variability – are well described with a function of latitude. A Gaussian filter with a standard deviation of $5°$ latitude is used to find a best-fit between observations excluding anomalous sites. The seasonal H_2 signal does not depend significantly on zonal variations in local deposition.

Neglecting the trend of increasing H_2 concentrations – which are propagated to the planetary scale due its long atmospheric lifetime – and considering the dominant role of surface uptake in the H_2 sink, this meridional gradient (Fig. 1b) suggests a net down gradient mixing from the tropics to the NH high-latitudes contrasted with approximately no meridional gradient between the tropics and SH mid and high-latitudes. This supports the assumption that the deposition into soils is dominated by the larger land area of the NH, where this soil sink exceeds anthropogenic emissions and the net source of H_2 from atmospheric chemistry (Paulot et al., 2021).

Outside the tropics, the first harmonic of the seasonal oscillation peaks in the late spring to early summer – between April and June – in the NH, and in late summer – late February – in the SH. The amplitude of this harmonic increases with latitude in the NH, and is reduced in the deep tropics compared with the subtropics, reflecting the different seasonality in the tropics compared with temperate regions. Figure 3b shows a spread in the phase of the seasonality in the NH between 10 and $45°$N of about 2 months, from late April to late June. There are a cluster of measurements where the first harmonic peaks in June – later in summer in the NH, more similar to the late summer peak in the SH (red squares, Figs. 1,3). These sites are spread zonally, and have an amplitude of this first harmonic, as well as a second harmonic, of seasonality consistent with other observations in the NH (Figs. 3a,c,d).

We define a reference monthly mean H_2 mixing ratio, r_{ref}, as the sum of the observed annual mean state and first and second harmonics fit to the observations with a Gaussian filter with $\sigma = 5°$lat excluding stations with anomalous signals. This reference H_2 signal isolates the dominant signal from noise and inter-annual variability, the decomposition of r_{ref} recovers the
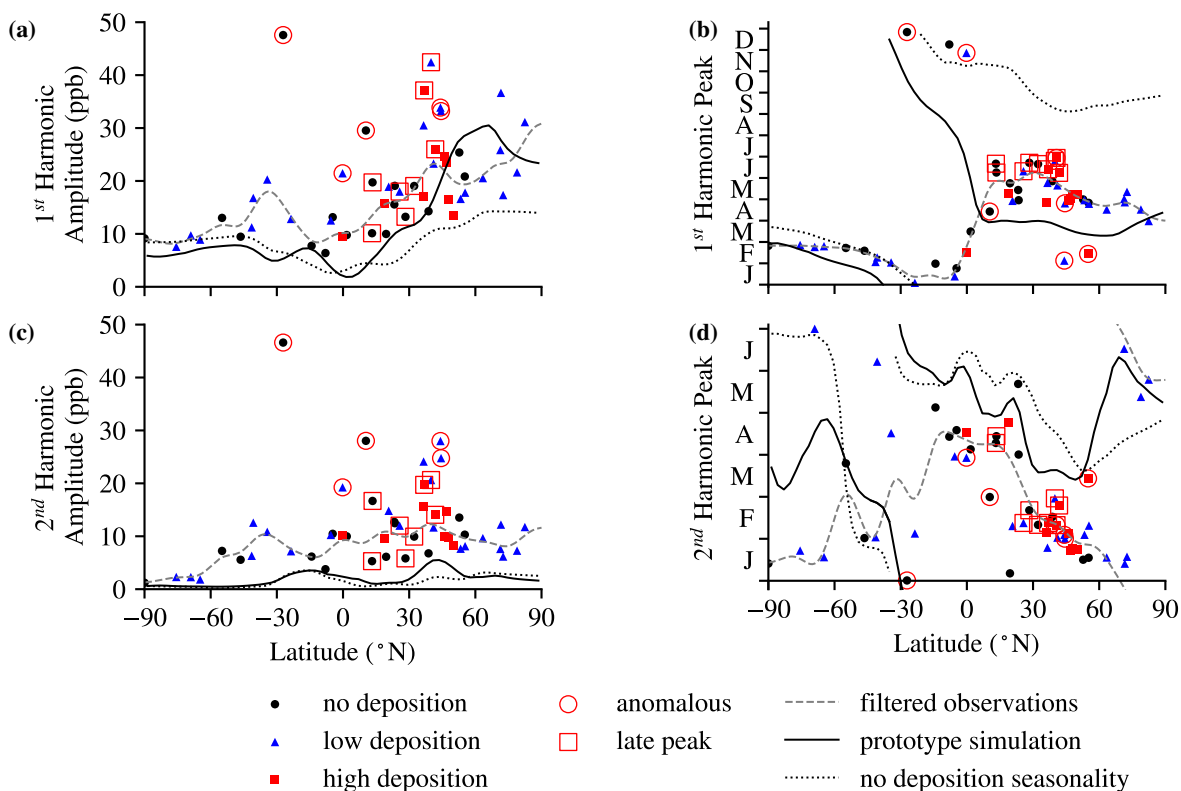
Figure 3. Seasonality of the 2012-2018 H_2 mixing ratio at surface measuring sites (symbols, see Fig. 1) (Pétron et al., 2023), the near-surface conditions of a simulation using the prototype deposition scheme (solid line, see Tab. 1) and using the annual mean deposition velocity of this scheme (dotted line): (**a**) and (**c**) the amplitudes of the first and second harmonics of the seasonal oscillation (A_1 and A_2); and (**b**) and (**d**) the phase of the peak of the first and second harmonics of the seasonal oscillation (Φ_1 and Φ_2). Note, the pattern for Φ_2 over the first six months repeats over the last six months. Filtered observations (grey dashed line) is a fit to the observational data excluding anomalous stations using a Gaussian filter with $\sigma = 5°$lat.

best-fit to the 2012-2018 surface observations: in the annual mean (grey dashed, Fig. 1b); the first harmonic of the seasonality (grey dashed, Figs. 3a,b); and the second harmonic (grey dashed, Figs. 3c,d).

The importance of deposition seasonality is indicated in Fig. 3: a simulation without deposition seasonality (dotted line) fails to reproduce key features of the planetary H_2 seasonality. In the simulation with H_2 seasonality driven by emissions and atmospheric chemistry (solid line), in both hemispheres H_2 peaks in late-summer to early-autumn – February-March in SH and August-September in NH – with similar zonal-mean peak amplitude 10-15 ppb to the observations in the mid-latitudes. Seasonally varying deposition is required for NH H_2 to peak earlier in the year and to resolve the distinct latitude bands of peak seasonality.

Table 1. Summary of deposition schemes used and devised in this study.

Deposition Scheme	Description	Experiments
prototype scheme	proportional to the leading terms in Bertagni et al. (2021): $$W_{prototpye} = k\,f(s)\,h(T),$$ where k is a constant to scale annual deposition to the multi-model mean from Sand et al. (2023)	prototype simulation (Figs. 1,3,7,8,10)
best-fit 1 (BF1)	deposition anomaly that reproduces observed seasonality: found as an anomaly from a simulation with the annual mean prototype deposition scheme as a basic state	BF1 (Figs. 7,8)
best-fit 2 (BF2)	prototype scheme perturbed with an anomaly: an anomaly is found from a simulation with the monthly varying prototype scheme as the basic state, a small (0 Tg annual mean) emissions perturbation is used to ensure $W_{BF2} \geq 0$	BF2 (Figs. 9,10)
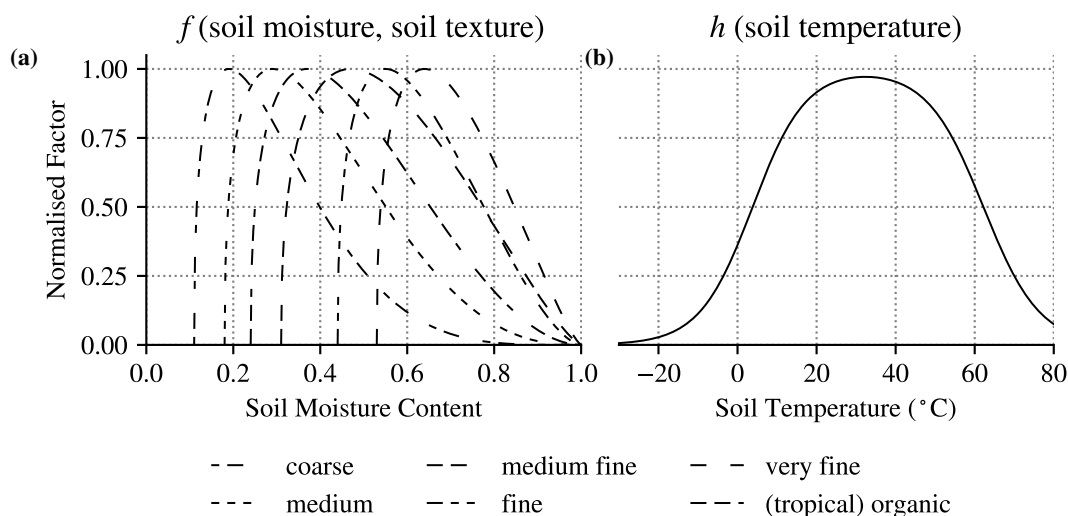
Figure 4. Normalised soil deposition rate factors (Ehhalt and Rohrer, 2011, Bertagni et al., 2021): **(a)** f for different soil textures used in ERA5 (Tab. 2); and **(b)** h.

Table 2. Mapping of ERA5 soil textures to the Bertagni et al. (2021) soil parameters. The *Medium* and *Medium fine* textures dominate over the land surface.

	ERA5 Soil Texture	Bertagni et al. (2021) Soil Texture
1:	Coarse	Sand
2:	Medium	Sandy loam
3:	Medium fine	Silt
4:	Fine	Sandy clay
5:	Very fine	Clay
6:	Organic	Loam
7:	Tropical Organic	Loam

3 A Prototype Deposition Scheme

Despite H_2 oxidising bacteria comprising an estimated $< 1\%$ of soil bacterial biomass (Khdhiri et al., 2015), they are ubiqui-
tously distributed in soils (Schlegel, 1974, Greening et al., 2016; Ji et al., 2017). Recently, Bertagni et al. (2021) formulated
the uptake of atmospheric H_2 – constrained by the rate of gas diffusion into soil and its microbial activity – as functions of soil
type, temperature and moisture, and without including a function of soil carbon, to derive a global model for H_2 deposition.

To simplify our analysis of the dominant drivers of seasonality in H_2 deposition we implement a prototype scheme that
isolates the deposition rate seasonality due to the soil moisture and soil temperature limiting terms (Ehhalt and Rohrer, 2011;
Ehhalt and Rohrer, 2013; Bertagni et al., 2021): $f(s)$ and $h(T)$ respectively, where s is soil moisture and T is soil temperature.
Ehhalt and Rohrer (2013) and Bertagni et al. (2021) identified the importance of high-frequency fluctuations in their deposition
models – particularly as a product of the changing soil moisture depth-profile through cycles of precipitation and drying. As
we base our constraints on the planetary scale seasonality at lower frequencies of 1-2 yr^{-1}, we drive f and h with monthly
mean ERA5 soil moisture in the top 7 cm and skin temperature, and scale the deposition rate with a constant to close the H_2
budget as in Sand et al. (2023) (summarised in Tab. 3).

Suppressed H_2 uptake has been measured in soils at low and high moisture contents (Conrad and Seiler, 1981), yet Bertagni
et al. (2021) emphasise the continued lack of quantitative observations for how soil biological activity varies with soil moisture.
In lieu of this data, they provide an adaptable model which constrains the soil moisture limiting function with the soil matric
potential for different soil textures. Accepting this persistent difficulty, we define $f(s)$ (Fig. 4a) as a mapping of that defined
function to the ERA5 set of soil textures (Tab. 2).

We choose $h(T)$ as the normalised soil temperature dependence across H_2 removal experiments that was defined by Ehhalt
and Rohrer (2011) (Fig. 4b), where H_2 removal occurs from temperatures as low as $-20°C$, increases following a Fermi
distribution to a peak at around $30°C$ (cf. Smith-Downey et al., 2006), and is limited quickly for temperatures higher than
$40°C$.

130

135

140

145

4 Model Formulation

Analysis of the 2012-2018 observational data for H_2 mixing-ratio (from Pétron et al., 2023) showed that the mean, and first and second annual harmonics, of the H_2 distribution (Figs. 1b and 3a,b,c,d) are well described with a function of latitude. Additionally, we note the long lifetime of H_2 compared with timescales of horizontal mixing in the atmosphere (e.g. Pierrehumbert and Yang, 1993) indicating that H_2 is reasonably well mixed across zonal bands.

Therefore, we attempt to simulate a planetary H_2 signal in a simple 2D (latitude-height) model with monthly-varying zonal-mean emissions, atmospheric loss and production, soil deposition, and transport integrated with a 4th order Runge-Kutta method, with 30-day months and 4 steps per day. The latitude-height model comprises 64 equally spaced latitude bands with 3-layers representing the lower, middle and upper troposphere, for which we assume fixed pressure boundaries at 1000, 800, 600 and 150 hPa. The simplicity of the model is prioritised such that simulations carry a low computational cost and differences resulting from the model configurations may be readily identified.

4.1 Emissions of H_2

We constrain the total H_2 emissions and production and destruction by atmospheric chemistry to match the multi-model average fluxes estimates in Sand et al. (2023) from six models driven by prescribed boundary layer H_2 and CH_4 concentrations (summarised in Tab. 3). In Sand et al. (2023) total H_2 emissions were estimated as the residual in offline calculations considering simulated atmospheric H_2 production and destruction, and estimated H_2 deposition. They found in an inter-model mean of 35.7 ± 16.3 Tg yr^{-1} (summarised in Tab. 3 from Sand et al., 2023), which corresponds with the estimate of 1995-2015 average H_2 emissions of Paulot et al. (2021): 29.9-37.1 Tg yr^{-1}.

We set annual H_2 emissions to 35.7 ± 16.3 Tg, of which 7.8 Tg are monthly varying biomass burning emissions with the *input4MIPs* estimate (Marle et al., 2017). The remaining emissions from anthropogenic sources and nitrogen fixing are implemented using the monthly mean signals from Paulot et al. (2021) in their respective proportions, but requiring a c.+20% scaling: 17.1 Tg and 10.8 Tg respectively. Emissions are shown in 5a,b.

4.2 Atmospheric Chemistry of H_2

As shown in Figs. 1b and 3 the prototype simulation (black line) captures much of the observed H_2 distribution and seasonal variation (symbols) at the surface, and due to the small amplitude of seasonal variability compared with the annual mean H_2 mixing ratio, the H_2 concentrations in the initial prototype simulation and simulations that achieve a best-fit to observations will agree to within a few percent. While in reality loss fluxes are proportional to the H_2 mixing ratio, the close agreement permits a choice of atmospheric production and loss fluxes that do not depend on the H_2 mixing ratio in each simulation: the fluxes for production and destruction by atmospheric chemistry are taken from a simulation with the UKCA model with imposed H_2 mixing ratios at the boundary layer used in Sand et al. (2023). These fluxes are close to the multi-model mean in that study, but are scaled by a small amount such that the fluxes used in this study align with the atmospheric H_2 budget summarised in Tab. 3. Net chemical fluxes are shown in Fig. 5c.
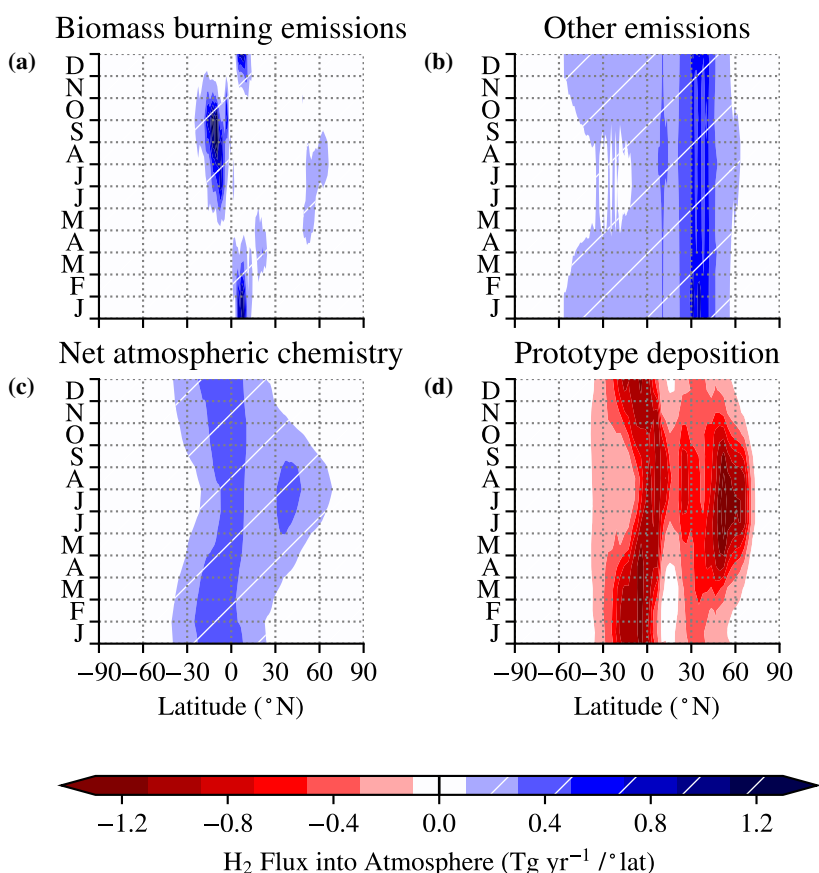
Figure 5. Different H_2 fluxes into the model: (**a**) emissions from biomass burning (from Marle et al., 2017); (**b**) other emissions including from combustion from fossil fuels and nitrogen fixing in soils and oceans (based on Paulot et al., 2021; Sand et al., 2023); (**c**) net production minus destruction by atmospheric chemistry (from Sand et al., 2023); and (**d**) zonal mean deposition with prototype scheme.

4.3 Atmospheric Transport of H_2

An idealised transport scheme is implemented as a monthly mean overturning in the troposphere and an empirically tuned representation of mixing. To ensure mass conservation in the overturning scheme, we first calculate a streamfunction from the monthly mean meridional overturning in ERA5 data over the period 2010-2020 (see Hersbach et al., 2020). Idealised representations of horizontal and vertical mixing as constant rates between layers and zonal bands are tuned to reproduce the meridional gradient in SF_6 from observations in the *World Data Centre for Greenhouse Gases* dataset from di Sarra et al. (2023) for simulations driven with *Emissions Database for Global Atmospheric Research* SF_6 emissions from Crippa et al. (2023).

Table 3. Summary of annual mean H_2 fluxes input to the model from: † Sand et al. (2023) mean over six fixed boundary layer concentration driven models with estimated emissions and a standard-deviation over the six models; ∗ the emissions from biomass burning of the total emissions from Marle et al. (2017).

	Mean (Tg yr^{-1})	Inter-Model σ (Tg yr^{-1})
Atmosphere Production †	46.8	7.4
Atmosphere Loss †	−25.2	3.2
Estimated Total Emissions †	35.7	16.3
Biomass Burning Emissions ∗	7.8	-

5 A Best-Fit Deposition Scheme

190

The remaining H_2 flux in the model is through deposition to soils – plotted for a simulation with the prototype deposition scheme in Fig. 5d. The prototype deposition scheme and each term may be decomposed into an annual mean state and a seasonality,

$$fh = \overline{fh} + (fh)', \tag{3}$$

195
$$f = \overline{f} + f', \tag{4}$$
$$h = \overline{h} + h', \tag{5}$$

where the over-bar refers to an annual mean, spatially varying field, and dashed fields are the seasonality. Figure 6 shows that the coefficient of variation – the ratio of the temporal standard deviation to the mean at each latitude – of f and h are distinct functions of latitude latitude, such that throughout most latitudes either $|f'| \ll \overline{f}$ or $|h'| \ll \overline{h}$ wherever there is strong

200 seasonality in the other term. This result shows that in most cases the cross-term $|f'h'| \ll \overline{fh}$, such that

$$\overline{fh} \approx \overline{f}\,\overline{h}, \tag{6}$$

and as a consequence,

$$fh - \overline{fh} \approx \left(\overline{f}h(T) - \overline{fh}\right) + \left(f(s)\overline{h} - \overline{fh}\right), \tag{7}$$

where the seasonality due to variations in soil moisture and the seasonality due to variation in soil temperature may be separated.

205 The seasonality of the deposition is then calculated as the product of the seasonality of the zonally integrated deposition velocity and r_{ref}, the signal of observed H_2 mixing ratios. This is shown in Fig. 7a.

An anomaly to the net surface flux is constructed of a perturbation to the prototype emissions and a perturbation to the prototype deposition scheme. We first identify the latitude-time signal of a deposition scheme that captures the best-fit to the seasonality of the observations independent of the seasonality of the prototype deposition scheme. This is the best-fit anomaly,

210 BF1 (Tab. 1), required to reproduce r_{ref} from a model with a basic deposition state taken as the annual mean deposition velocity of the prototype scheme, $\overline{fh}$. BF1 is calculated as the average rate of relaxation of a number of small Newtonian
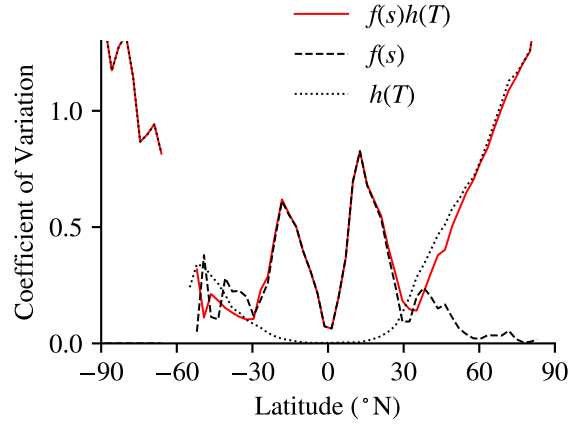
Figure 6. Coefficient of variation for the zonal mean of the prototype deposition scheme (red) and terms f (dashed) and h (dotted).

relaxations, R, towards r_{ref} through each month of integration. This is found in an inverted version of the model, where the H$_2$ mixing ratio in the lower layer, r, changes as

$$\frac{\partial}{\partial t} r = S + M - r\overline{fh} - R,\tag{8}$$

where

$$S = E + P + rD \tag{9}$$

represents emissions, E, and atmospheric chemistry production, P, and destruction, rD, M represents mixing, and the relaxation term

$$R = \delta_R(r - r_{ref}),\tag{10}$$

where $\delta_R \ll 1$ is a constant chosen such that r relaxes sufficiently close to r_{ref} by the end of the month, but allows steady adjustment and mixing of r over that period. Note, in this experiment, in the lower layer the seasonality in r is much smaller than the annual mean such that $|r - r_{ref}| \ll \bar{r}$, and $\sim 70\%$ of the total H$_2$ sink is by deposition into the soil (Sand et al., 2023) such that $rD \ll r\overline{fh}$, the net chemistry is assumed to be captured with the same monthly varying flux in each test.

We compare BF1 (Fig. 7b) to the seasonality of the prototype deposition scheme and its decomposed terms (Figs. 7a,c,d). The prototype scheme seasonality, $(fh)'$, reproduces some key features of BF1. In particular, the seasonality due to soil temperature captures the strong seasonality of BF1 in the NH mid-latitudes, which has been identified in microbial laboratory studies (Smith-Downey et al., 2006). Alternately, the seasonality driven by soil moisture changes is dominant in the tropics.
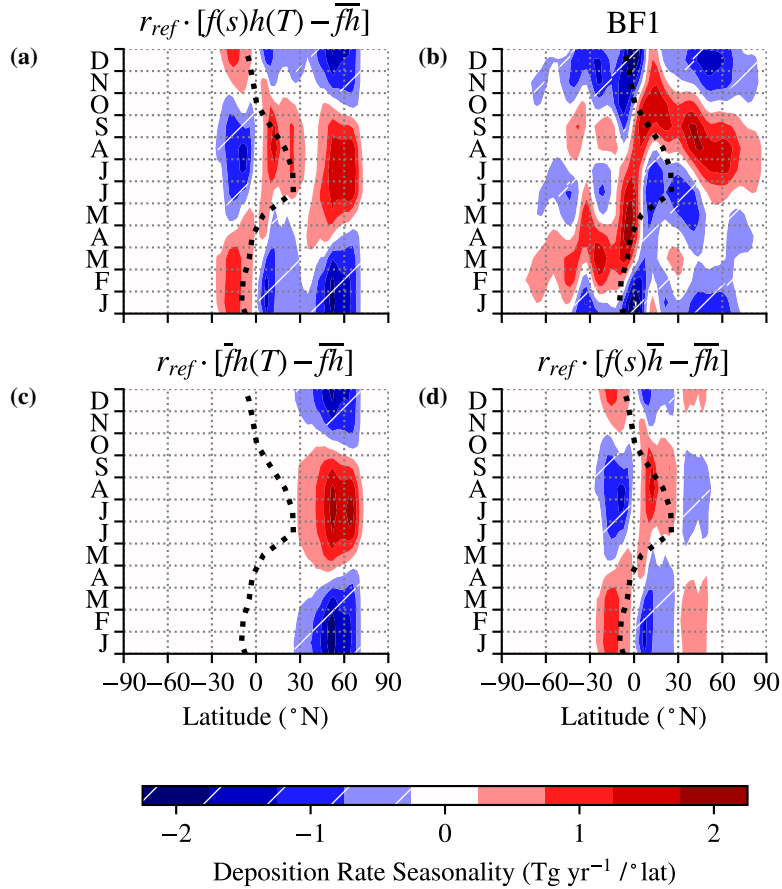
Figure 7. Deposition rate seasonality (shaded) for: (**a**) the prototype deposition scheme multiplied by near-surface mixing ratios of this simulation; (**b**) BF1 from $\overline{fh}$ found in the inverted model; Panels **c** and **d**) the prototype deposition scheme with isolated monthly variation that depend only on h and f respectively (Equation 7). In each (the ITCZ migration (black dots) is included as the order 10 precipitation centroid (from ERA5 2010-2020) between 20°S and 20°N following Adam et al. (2016).

To analyse how adjustments to the seasonality of the prototype deposition scheme affect results we define the ratio of the RMS error between the seasonality of an adjusted deposition scheme and BF1 to the RMS seasonality of BF1 at each latitude:

$$R_{BF}(\alpha, \Delta t) = \frac{\sqrt{\int_t^{t+1 \text{ year}} \left(r_{ref}^{-1} \text{BF1} - \alpha W'(t' - \Delta t) \right)^2 dt'}}{\sqrt{\int_t^{t+1 \text{ year}} \left(r_{ref}^{-1} \text{BF1} \right)^2 dt'}}, \tag{11}$$

230   where the adjusted deposition seasonality $\alpha W'(t - \Delta t)$ is the seasonality of the prototype scheme, $(fh)'$, scaled by a factor α and offset in time by Δt. This ratio indicates how well the adjusted deposition scheme performs at reproducing the best-fit deposition scheme: $R_{BF} = 0$ occurs where the adjusted scheme locally reproduces the best-fit scheme; $R_{BF} = 1$ occurs if
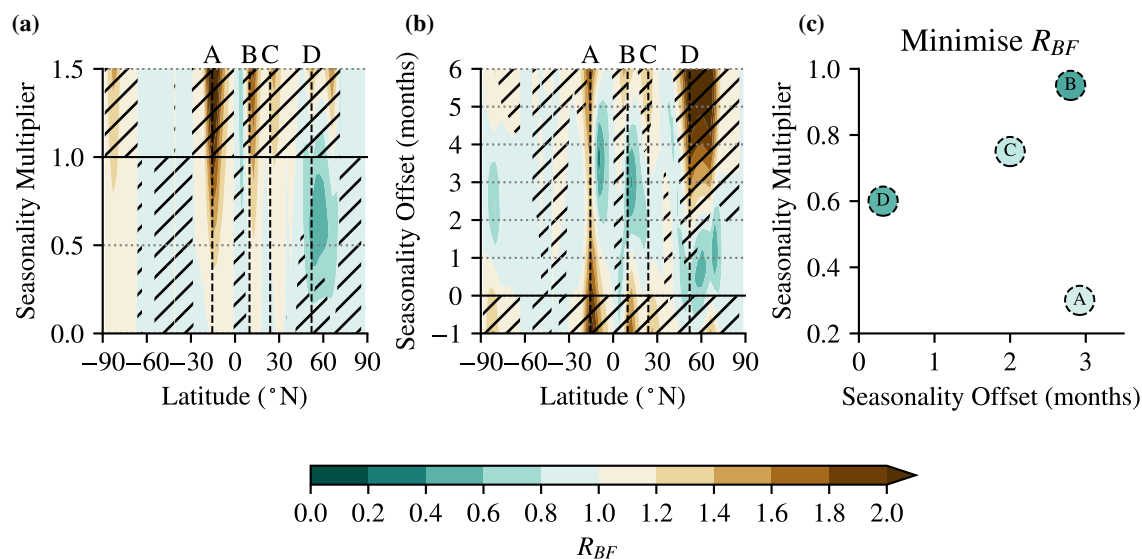
Figure 8. The ratio R_{BF} (Equation 11) measuring how well adjusted versions of the prototype deposition scheme perform at reproducing the best-fit deposition scheme. (**a**) the prototype deposition seasonality is scaled by a multiplier, α; (**b**) the deposition seasonality is offset in time by Δt; and (**c**) minimum R_{BF} achieved when α and Δt are varied at the latitudes of peaks in deposition seasonality in the prototype scheme (annotated A-D in each panel). Hatches indicate where the adjusted deposition scheme performs worse than the prototype scheme.

the adjusted scheme performs as well as the annual mean prototype deposition scheme, $\overline{fh}$; and $R_{BF} > 1$ indicates that the adjusted scheme performs worse than $\overline{fh}$.

235   In Fig. 8a the seasonality of fh only substantially reproduces BF1 where the strength of its seasonality is decreased in the temperate NH between 45-70°N. Alternately, in Fig. 8b, fh better reproduces BF1 scheme when it includes a lag of 2-4 months in the tropics, or half a month later in the NH mid-latitudes.

    In Fig. 8c the latitudes of peak amplitude of seasonality in the prototype scheme are isolated for optimised agreement with BF1 under adjustments to the seasonality multiplier and offset. In both deep tropical peaks (A,B), better agreement occurs for

240   a lag of ≈ 3 months. Additionally, the strongest agreement occurs for a weaker seasonality in the SH tropical peak (A). In the NH, better agreement is achieved where this lag and the amplitude of the seasonality of the peaks are decreased with increasing latitude; the peak at 52°N (D) agrees well with BF1 for a ~ 1 week lag and a 60% multiplier.

6   Contribution from Emissions and Chemical Production and Destruction

We have shown that the seasonality of the monthly varying prototype deposition scheme, fh, captures the key features of a

245   scheme that represents a best-fit for the observed seasonality independent of the seasonality of the prototype scheme, BF1. Given that similar seasonal signals to the biophysics based seasonality of the prototype scheme are independently reproduced

by BF1 we examine a second best-fit scheme, BF2 (Tab. 1), derived as a perturbation from the full monthly varying prototype scheme. In this case, Equation 8 becomes

$$\frac{\partial}{\partial t} r = S + M - rfh - R, \tag{12}$$

250 where S in unchanged but the mixing, M, and relaxation, R, terms respond to the change $\overline{fh} \to fh$. Like BF1, BF2 is calculated from the flux anomaly (Fig. 9a) contained in R and required to resolve r_{ref}.
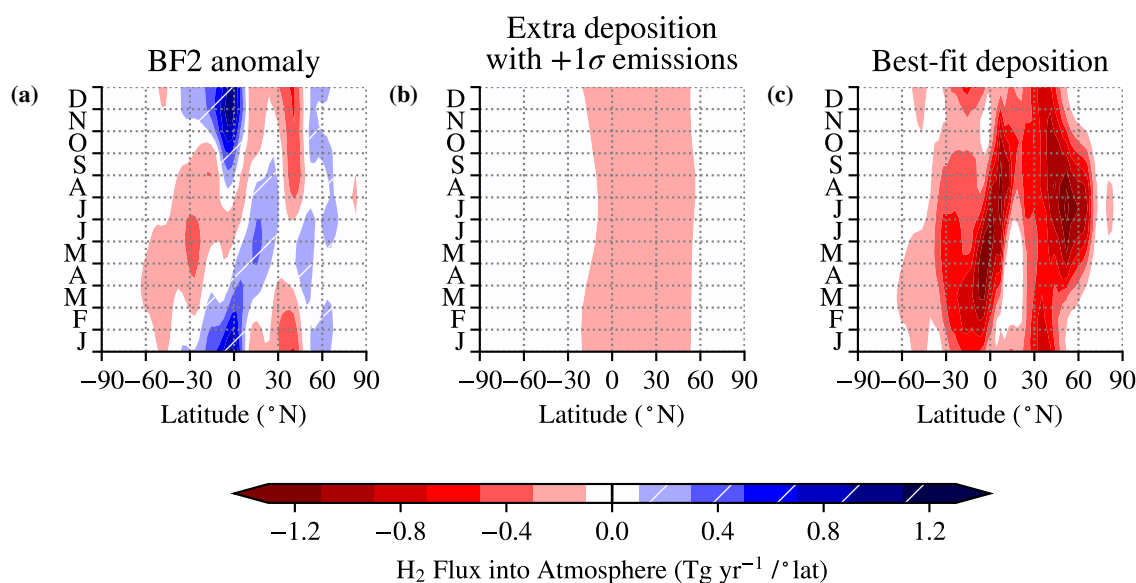
Figure 9. Different H_2 fluxes into the model: **(a)** BF2 anomaly into lower layer to reproduce observations versus a simulation using the prototype deposition scheme; **(b)** anomaly change per $+1\sigma$ change in 'other emissions'; and **(c)** 'best-fit deposition' under the prototype deposition scheme perturbed by BF2.

Due to the large inter-model spread in estimated H_2 emissions (Tab. 3, Sand et al., 2023), it is necessary to consider how much of the BF2 anomaly may be explained by the emissions (Figs. 5a,b) and chemistry (Fig. 5c) schemes. The BF2 anomaly is strongest in the tropics and subtropics with a net upwards flux peaking south of the Equator in November-December and 255 spreading into the northern tropics during the NH summer. This upwards flux is similar to the source from biomass burning, where other studies have used stronger emissions for biomass burning than the inputs4MIPS (Marle et al., 2017) scheme (e.g. Novelli, 1999; Sanderson et al., 2003; Price et al., 2007; Xiao et al., 2007). However it also captures a weakening of the high deposition in the prototype deposition scheme driven by increases in f following the migration of the ITCZ (Fig. 6d). Combined with the stronger deposition during the winter in the subtropics in both hemispheres, this structure captures an offset 260 in the prototype deposition scheme of around 3 months as seen earlier for BF1 (Fig. 8c).

Alternatively, the upwards flux component of this anomaly may partly be explained through an intensification of emissions due to nitrogen fixing or net production by chemical processes during the summer in the subtropics and tropics. Increasing the

intensity of the non-biomass burning H_2 emissions by one standard deviation of the Sand et al. (2023) inter-model emissions estimate requires enhanced deposition with a maximum of around 0.2 Tg yr^{-1}/°lat focused in the NH mid-latitudes, and
265   peaking in both hemispheres between December and February (Fig. 9b).

7   Effect on H_2 Lifetime of the Perturbed Scheme

To examine the effect of changing the prototype deposition scheme to the best-fit deposition scheme, BF2, we conduct a series of H_2 perturbation experiments. Timescales of deposition into the soil for small H_2 perturbations $r' \ll r_{ref}$ are communicated as a lifetime for comparison with the approximately 3.4 year soil deposition lifetime calculated by Sand et al. (2023). For
270   sufficiently small perturbations, we assume the chemistry fluxes are unchanged, and the anomalous flux is dominated by the soil flux (see Prather and Holmes, 2013). Likewise, we assume the differences between experiments with the prototype deposition scheme and BF2 are not obscured by using the same chemistry fluxes.

From the soil deposition timescales, an approximate total lifetime, τ_{total}, is calculated as the harmonic sum of the lifetime due to chemical loss in the atmosphere $\tau_{atmchem} = 7.7$ years from Sand et al. (2023), and soil deposition timescales for each
275   perturbation, with an approximate scaling factor $1000/850$ because the 2D model only extends to 150 hPa rather than the top of atmosphere, assuming that vertical variation in H_2 mixing ratios in the upper 150 hPa of the atmosphere are similar to those modelled between 1000 and 150 hPa (e.g. Warwick et al., 2004),

$$\tau_{total}^{-1} \approx \tau_{atmchem}^{-1} + \left(\frac{1000 \text{ hPa}}{850 \text{ hPa}} \tau_{soil}^{\dagger,*} \right)^{-1}, \tag{13}$$

where $\tau_{soil}^{\dagger,*}$ are model timescales calculated in different experiments.
280   In two perturbation experiments, perturbations to H_2 are: $\dagger$ as $+1$ ppb throughout the simulated atmosphere initiated for each month (Fig. 10a); and $*$ as $+0.1$ Tg in the lower 200 hPa layer through a continuum of latitude bands, and initiated at 0, 90, 180 and 270 days to sample the sensitivity of the soil lifetime to the season of the emission (Fig. 10b). A soil lifetime is then calculated from the decay of each perturbation after one year.

In the prototype scheme, the SH deposition peaks at 10-20°S around 1 month into the year (Fig. 7b). Whereas the best-fit
285   SH deposition occurs in extended periods spreading northwards across the equator from 2-9 months and in the SH subtropics into the winter (Fig. 9c). In the NH, BF2 has a similar temporal signal as the prototype scheme, but peaking 1-2 months later in the year as shown in Fig. 8b.

In simulations using the prototype scheme, a whole-troposphere H_2 perturbation has the longest soil lifetime, τ_{soil}, when initialised around 150 days into the year – as a product of the seasonal high mixing ratio in the NH subtropics observed in Fig.
290   1b. τ_{soil} has a minimum for perturbations initialised around 30 days, when there is a high rate of deposition in the SH, but is half a year out of phase with the peak deposition, which is concentrated in the NH (Fig. 7b).

Under BF2, τ_{soil} is decreased for perturbations initialised at the start of the year and increased for perturbations initialised around 180 days. In general, perturbations initialised around 180 days have more time to mix and react in the atmosphere before deposition.

295   There is a gradient of longer τ_{soil} for perturbations initialised near the surface in the SH to shorter τ_{soil} for those initialised in the NH reflecting the greater soil sink in the NH. For perturbations initialised at low-latitudes, the seasonality of τ_{soil} corresponds with those of whole troposphere perturbations. However, this is inverted for perturbations initialised in the extra-tropical NH where τ_{soil} is longest for perturbations initialised in the autumn and winter. The longer soil deposition timescale in the SH corresponds with a result of Derwent (2023), who identified a monotonically decreasing GWP for H_2 emissions

300   sources from the SH mid-latitudes to the NH mid-latitudes.

The same pattern is largely reproduced for simulations using BF2, but with a weaker meridional gradient. Quadratic fits of τ_{soil} against equal area intervals (sin of the perturbation latitude, λ) result in $\tau_{soil} = 2.8 \pm 0.3$ years at the equator, with a weaker first degree gradient of -0.9 ± 0.2 years with BF2 compared with -1.2 ± 0.3 years with the prototype scheme, and a weaker change in this negative gradient with latitude. The BF2 deposition scheme allows any H_2 emission in the SH to

305   more quickly deposit into soils, even where this emission occurs far south of $30°$S – despite strong deposition in BF2 being constrained north of this latitude (Fig. 9c). This reflects how BF2 resolves the too high H_2 mixing ratios in the extra-tropical shown in Fig. 1b.
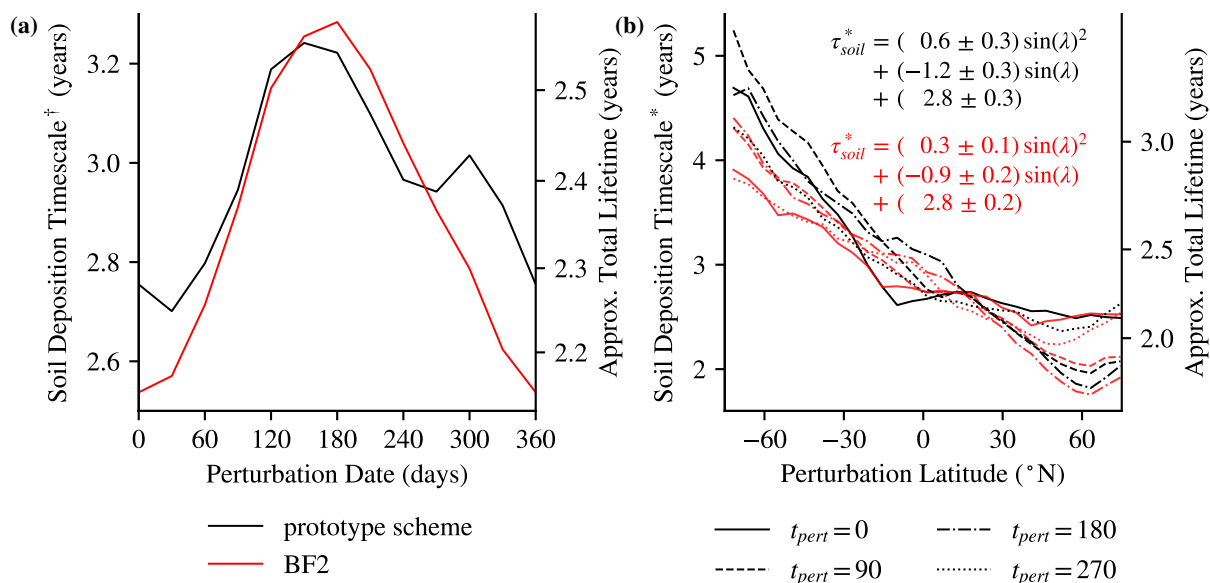
Figure 10. Soil timescales calculated from 1 year simulations with: (**a**) $\tau_{soil}^{\dagger}$ calculated with whole troposphere 1ppb perturbations initialised at a range of dates; and (**b**) τ_{soil}^{*} calculated with perturbations of 0.1 Tg in the lower 200 hPa in latitude bands – quadratic fits are made against sin latitude. In both cases the soil lifetime is underestimated as the atmosphere is only simulated though 1000-150 hPa and due to the relatively short simulation length; and in $*$ near surface perturbation configuration. Approximate τ_{total} is the harmonic sum of $\frac{1}{0.85}\tau_{soil}^{\dagger,*}$ and $\tau_{atmchem}$, which is assumed to have the constant value 7.7 years from Sand et al. (2023).

8 Conclusions

The methods we have discussed provide a toolbox to constrain the development of H_2 deposition schemes using empirical
310   observations of the zonal mean H_2 distribution and seasonality. In particular, we have identified the asymmetry in the seasonal
cycle of H_2 in the NH and SH. Without a seasonally varying soil uptake, zonal mean surface H_2 would peak with a similar am-
plitude during the late-summer to early-autumn in both the NH and SH extra-tropical regions; the seasonality of the deposition
induces a stronger amplitude and earlier peak in the NH H_2 signal.

  We have shown that a prototype deposition scheme based on the assumed leading physical-biological processes of soil H_2
315   uptake (Fig. 5d) is able to effectively capture some key features of the planetary H_2 distribution in the 2D model. Assuming the
annual-mean of this prototype scheme as a suitable basic deposition state, we then produced a 'best-fit' deposition scheme that
reproduces the planetary H_2 seasonality independent of the seasonality of the prototype scheme. Comparing the seasonality
of the best-fit scheme against the prototype scheme tested the accuracy of the seasonality of the prototype scheme. This
challenges the assumed deposition seasonality in the tropics, providing useful insight for where similar deposition schemes
320   should be revised to improve the accuracy in future H_2 modelling efforts.

  In the NH extra-tropics the prototype scheme performs well at reproducing the observed annual mean meridional gradient
and seasonality of surface H_2 mixing ratios. In the SH the prototype scheme results in too-high surface mixing ratios in the
annual mean, and differences in phase and a weak amplitude of the seasonality in the Southern tropics and subtropics. We find
that while the prototype scheme agrees with key features of the best-fit deposition scheme, the prototype deposition scheme
325   would better reproduce observations with a lag of $+3$ months in its seasonality in the tropics. Other sources of hysteresis on the
seasonality may be explained by dependence on: irreversible degeneration of free enzymes in soils where seasonal temperatures
fluctuate above $30°C$ (Chowdhury and Conrad, 2010); variations in the soil organic carbon content (King et al., 2008; Karbin
et al., 2024); or even the life-cycle of soil microbes (Meredith et al., 2014). Our results indicate that deeper investigations into
the H_2 flux in tropical soils are needed to build our understanding of the links between these soil microbial processes and the
330   planetary scale H_2 signal.

  A second best-fit deposition scheme was found as a perturbation to the monthly-varying prototype scheme (Fig. 9c). Both in
the prototype and best-fit deposition schemes there is both a strong seasonal and meridional dependence of the soil deposition
timescale for different configurations of H_2 perturbations. The choice of the deposition scheme also had a strong impact on the
meridional dependence of the soil lifetime for H_2 emissions.

335   When calculating the climate benefit of future hydrogen energy systems, such as by Hauglustaine et al. (2022), constraining
the H_2 surface flux may have a significant impact for the sensitive question of how accurately comprehensive models predict
the spatial dependence of environmental impacts from spurious H_2 emissions in regional industrial hydrogen projects (e.g.
Derwent, 2023). This is particularly important in the SH, where soil deposition timescales are shorter in simulations with the
best-fit scheme compared with the prototype scheme.

340 *Author contributions.* A. K. Tardito Chaudhri – ideation, analysis design, performing analysis, writing; and D. S. Stevenson – ideation, analysis design, writing.

Competing interests. No competing interests are present.

Acknowledgements. Hannah Bryant for UKCA chemistry outputs from earlier work (Sand et al., 2023); Fabien Paulot for estimated emissions files from earlier work (Paulot et al., 2021); those aforesaid and Richard Derwent, Saeed Karbin, Keith Shine and Joanne Smith for
345 helpful and motivating discussions. This work used JASMIN, the UK's collaborative data analysis environment (https://www.jasmin.ac.uk).

References

Adam, O., Bischoff, T., and Schneider, T.: Seasonal and interannual variations of the energy flux equator and ITCZ. Part I: Zonally averaged ITCZ position, J. Climate, 29, 3219–3230, 2016.

Bertagni, M. B., Paulot, F., and Porporato, A.: Moisture Fluctuations Modulate Abiotic and Biotic Limitations of H2 Soil Uptake, Global Biogeochemical Cycles, 35, e2021GB006 987, https://doi.org/10.1029/2021GB006987, 2021.

Chowdhury, S. P. and Conrad, R.: Thermal deactivation of high-affinity H2 uptake activity in soils, Soil Biology and Biochemistry, 42, 1574–1580, https://doi.org/https://doi.org/10.1016/j.soilbio.2010.05.027, 2010.

Conrad, R. and Seiler, W.: Decomposition of atmospheric hydrogen by soil microorganisms and soil enzymes, Soil Biology and Biochemistry, 13, 43–49, https://doi.org/https://doi.org/10.1016/0038-0717(81)90101-2, 1981.

Crippa, M., Guizzardi, D., Pagani, F., Banja, M., Muntean, M., Schaaf, E., Becker, W., Monforti-Ferrario, F., Quadrelli, R., Risquez Martin, A., Taghavi-Moharamli, P., Köykkä, J., Grassi, G., Rossi, S., Brandao De Melo, J., Oom, D., Branco, A., San-Miguel, J., and Vignati, E.: GHG emissions of all world countries, https://doi.org/10.2760/953322, jRC134504, 2023.

Derwent, R. G.: Global warming potential (GWP) for hydrogen: Sensitivities, uncertainties and meta-analysis, International Journal of Hydrogen Energy, 48, 8328–8341, https://doi.org/10.1016/j.ijhydene.2022.11.219, 2023.

di Sarra, A., Hall, B. D., Couret, C., Lunder, C., Rennick, C., Sweeney, C., Shin, D., Sferlazzo, D., Mondeel, D. J., Young, D., Cuevas, E., Meinhardt, F., Dutton, G. S., Nance, J. D., Mühle, J., Arduini, J., Pitt, J., TECHNOS, K., Tsuboi, K., Stanley, K., Gatti, L. V., Steinbacher, M., Vollmer, M., Hermansen, O., Fraser, P., Krummel, P., Rivas, P., Weiss, R. F., Wang, R., Chiavarini, S., Piacentino, S., O'Doherty, S., Reimann, S., Montzka, S. A., Park, S., Saito, T., and Lan, X.: All SF6 data contributed to WDCGG by GAW stations and mobiles by 2023-09-13, https://doi.org/10.50849/WDCGG_SF6_ALL_2023, 2023.

Ehhalt, D. H. and Rohrer, F.: The tropospheric cycle of H2: A critical review, https://doi.org/10.1111/j.1600-0889.2009.00416.x, 2009.

Ehhalt, D. H. and Rohrer, F.: The dependence of soil H2 uptake on temperature and moisture: a reanalysis of laboratory data, Tellus B: Chemical and Physical Meteorology, https://doi.org/10.1111/j.1600-0889.2011.00581.x, 2011.

Ehhalt, D. H. and Rohrer, F.: Deposition velocity of H2: A new algorithm for its dependence on soil moisture and temperature, Tellus, Series B: Chemical and Physical Meteorology, 65, https://doi.org/10.3402/tellusb.v65i0.19904, 2013.

Esquivel-Elizondo, S., Hormaza Mejia, A., Sun, T., Shrestha, E., Hamburg, S. P., and Ocko, I. B.: Wide range in estimates of hydrogen emissions from infrastructure, Frontiers in Energy Research, 11, https://doi.org/10.3389/fenrg.2023.1207208, 2023.

Greening, C., Biswas, A., Carere, C., et al.: Genomic and metagenomic surveys of hydrogenase distribution indicate H2 is a widely utilised energy source for microbial growth and survival, ISME J, 10, 761–777, https://doi.org/10.1038/ismej.2015.153, 2016.

Hauglustaine, D., Paulot, F., Collins, W., Derwent, R., Sand, M., and Boucher, O.: Climate benefit of a future hydrogen economy, Communications Earth and Environment, 3, https://doi.org/10.1038/s43247-022-00626-z, 2022.

Hauglustaine, D. A. and Ehhalt, D. H.: A three-dimensional model of molecular hydrogen in the troposphere, Journal of Geophysical Research Atmospheres, 107, ACH 4–1–ACH 4–16, https://doi.org/10.1029/2001JD001156, 2002.

Hersbach, H., Bell, B., Berrisford, P., Hirahara, S., Horányi, A., Muñoz-Sabater, J., Nicolas, J., Peubey, C., Radu, R., Schepers, D., Simmons, A., Soci, C., Abdalla, S., Abellan, X., Balsamo, G., Bechtold, P., Biavati, G., Bidlot, J., Bonavita, M., De Chiara, G., Dahlgren, P., Dee, D., Diamantakis, M., Dragani, R., Flemming, J., Forbes, R., Fuentes, M., Geer, A., Haimberger, L., Healy, S., Hogan, R. J., Hólm, E., Janisková, M., Keeley, S., Laloyaux, P., Lopez, P., Lupu, C., Radnoti, G., de Rosnay, P., Rozum, I., Vamborg, F., Vil-

laume, S., and Thépaut, J.-N.: The ERA5 global reanalysis, Quarterly Journal of the Royal Meteorological Society, 146, 1999–2049, https://doi.org/https://doi.org/10.1002/qj.3803, 2020.

Ji, M., Greening, C., Vanwonterghem, I., et al.: Atmospheric trace gases support primary production in Antarctic desert surface soil, Nature,
385   552, 400–403, https://doi.org/10.1038/nature25014, 2017.

Karbin, S., Drewer, J., Dean, J. F., et al.: Modelling Hydrogen Uptake in Soil: Exploring the Role of Microbial Activity, ESS Open Archive, https://doi.org/10.22541/essoar.172347413.30006667/v1, preprint, 2024.

Khdhiri, M., Hesse, L., Popa, M. E., Quiza, L., Lalonde, I., Meredith, L. K., Röckmann, T., and Constant, P.: Soil carbon content and relative abundance of high affinity H2-oxidizing bacteria predict atmospheric H2 soil uptake activity better than soil microbial community
390   composition, Soil Biology and Biochemistry, 85, 1–9, https://doi.org/https://doi.org/10.1016/j.soilbio.2015.02.030, 2015.

King, G. M., Weber, C. F., Nanba, K., Sato, Y., and Ohta, H.: Atmospheric CO and Hydrogen Uptake and CO Oxidizer Phylogeny for Miyake-jima, Japan Volcanic Deposits, Microbes and Environments, 23, 299–305, https://doi.org/10.1264/jsme2.ME08528, 2008.

Marle, M. J. V., Kloster, S., Magi, B. I., Marlon, J. R., Daniau, A. L., Field, R. D., Arneth, A., Forrest, M., Hantson, S., Kehrwald, N. M., Knorr, W., Lasslop, G., Li, F., Mangeon, S., Yue, C., Kaiser, J. W., and Werf, G. R. V. D.: Historic global biomass burning emissions for
395   CMIP6 (BB4CMIP) based on merging satellite observations with proxies and fire models (1750-2015), Geoscientific Model Development, 10, 3329–3357, https://doi.org/10.5194/gmd-10-3329-2017, 2017.

Meredith, L. K., Rao, D., Bosak, T., Klepac-Ceraj, V., Tada, K. R., Hansel, C. M., Ono, S., and Prinn, R. G.: Consumption of atmospheric hydrogen during the life cycle of soil-dwelling actinobacteria, Environmental Microbiology Reports, 6, 226–238, https://doi.org/10.1111/1758-2229.12116, 2014.

400 NOAA Global Monitoring Laboratory: Air Sample Collection Using the Manual Portable Sampling Unit: Revision 1.6, https://gml.noaa. gov/ccgg/psu/manuals/psu_manual_1.6.pdf, accessed: 2024-06-27, 2005.

NOAA Global Monitoring Laboratory: Carbon Cycle Greenhouse Gases, https://www.gml.noaa.gov/dv/site/gmdsites.php?program=ccgg& projtable=1, accessed: 2024-06-27, 2024.

Novelli, P. C.: Molecular hydrogen in the troposphere: Global distribution and budget, Journal of Geophysical Research Atmospheres, 104,
405   30 427–30 444, https://doi.org/10.1029/1999JD900788, 1999.

Ocko, I. B. and Hamburg, S. P.: Climate consequences of hydrogen emissions, Atmospheric Chemistry and Physics, 22, 9349–9368, https://doi.org/10.5194/acp-22-9349-2022, 2022.

Patterson, J. D., Aydin, M., Crotwell, A. M., Petron, G., Severinghaus, J. P., and Saltzman, E. S.: Atmospheric History of H2 Over the Past Century Reconstructed From South Pole Firn Air, Geophysical Research Letters, 47, https://doi.org/10.1029/2020GL087787, 2020.

410 Paulot, F., Paynter, D., Naik, V., Malyshev, S., Menzel, R., and Horowitz, L. W.: Global modeling of hydrogen using GFDL-AM4.1: Sensitivity of soil removal and radiative forcing, International Journal of Hydrogen Energy, 46, 13 446–13 460, https://doi.org/10.1016/J.IJHYDENE.2021.01.088, 2021.

Paulot, F., Pétron, G., Crotwell, A. M., and Bertagni, M. B.: Reanalysis of NOAA H$_2$ observations: implications for the H$_2$ budget, Atmospheric Chemistry and Physics, 24, 4217–4229, https://doi.org/10.5194/acp-24-4217-2024, 2024.

415 Pierrehumbert, R. T. and Yang, H.: Global Chaotic Mixing on Isentropic Surfaces, Journal of Atmospheric Sciences, 50, 2462 – 2480, https://doi.org/10.1175/1520-0469(1993)050<2462:GCMOIS>2.0.CO;2, 1993.

Prather, M. and Holmes, C. D.: A perspective on time: loss frequencies, time scales and lifetimes, Environmental Chemistry, 10, 73–79, 2013.

Price, H., Jaeglé, L., Rice, A., Quay, P., Novelli, P. C., and Gammon, R.: Global budget of molecular hydrogen and its deuterium content: Constraints from ground station, cruise, and aircraft observations, Journal of Geophysical Research Atmospheres, 112, https://doi.org/10.1029/2006JD008152, 2007.

Pétron, G., Crotwell, A. M., Mund, J., Crotwell, M., Mefford, T., Thoning, K., Hall, B., Kitzis, D., Madronich, M., Moglia, E., Neff, D., Wolter, S., Jordan, A., Krummel, P., Langenfelds, R., and Patterson, J.: Atmospheric Hydrogen Dry Air Mole Fractions from the NOAA GML Carbon Cycle Cooperative Global Air Sampling Network, 2009-2021 [Data set]. NOAA GML CCGG Division, https://doi.org/10.5194/amt-2024-4, 2023.

Sand, M., Skeie, R. B., Sandstad, M., Krishnan, S., Myhre, G., Bryant, H., Derwent, R., Hauglustaine, D., Paulot, F., Prather, M., and Stevenson, D.: A multi-model assessment of the Global Warming Potential of hydrogen, Communications Earth and Environment, 4, https://doi.org/10.1038/s43247-023-00857-8, 2023.

Sanderson, M. G., Collins, W. J., Derwent, R. G., and Johnson, C. E.: Simulation of Global Hydrogen Levels Using a Lagrangian Three-Dimensional Model, 2003.

Schlegel, H. G.: Production, modification, and consumption of atmospheric trace gases by microorganisms, Tellus A: Dynamic Meteorology and Oceanography, https://doi.org/10.3402/tellusa.v26i1-2.9732, 1974.

Smith-Downey, N. V., Randerson, J. T., and Eiler, J. M.: Temperature and moisture dependence of soil H2 uptake measured in the laboratory, Geophysical Research Letters, 33, https://doi.org/10.1029/2006GL026749, 2006.

Warwick, N. J., Bekki, S., Nisbet, E. G., and Pyle, J. A.: Impact of a hydrogen economy on the stratosphere and troposphere studied in a 2-D model, Geophysical Research Letters, 31, https://doi.org/10.1029/2003gl019224, 2004.

Warwick, N. J., Archibald, A. T., Griffiths, P. T., Keeble, J., O'Connor, F. M., Pyle, J. A., and Shine, K. P.: Atmospheric composition and climate impacts of a future hydrogen economy, Atmospheric Chemistry and Physics, 23, 13 451–13 467, https://doi.org/10.5194/acp-23-13451-2023, 2023.

Xiao, X., Prinn, R. G., Simmonds, P. G., Steele, L. P., Novelli, P. C., Huang, J., Langenfelds, R. L., O'Doherty, S., Krummel, P. B., Fraser, P. J., Porter, L. W., Weiss, R. F., Salameh, P., and Wang, R. H. J.: Optimal estimation of the soil uptake rate of molecular hydrogen from the Advanced Global Atmospheric Gases Experiment and other measurements, Journal of Geophysical Research: Atmospheres, 112, https://doi.org/https://doi.org/10.1029/2006JD007241, 2007.

Yashiro, H., Sudo, K., Yonemura, S., and Takigawa, M.: The impact of soil uptake on the global distribution of molecular hydrogen: Chemical transport model simulation, Atmospheric Chemistry and Physics, 11, 6701–6719, https://doi.org/10.5194/acp-11-6701-2011, 2011.

Yonemura, S., Kawashima, S., and Tsuruta, H.: Carbon monoxide, hydrogen, and methane uptake by soils in a temperate arable field and a forest, Journal of Geophysical Research Atmospheres, 105, 14 347–14 362, https://doi.org/10.1029/1999JD901156, 2000.